Global Biogeochemical Cycles

Supporting Information for

Interannual and seasonal drivers of carbon cycle variability represented by the Community Earth System Model (CESM2)

William R. Wieder[1,2], Zachary Butterfield[3], Keith Lindsay[1],
Danica L. Lombardozzi[1], Gretchen Keppel-Aleks[3]

[1] Climate and Global Dynamics Laboratory, National Center for Atmospheric Research, Boulder, CO 80307, USA.

[2] Institute of Arctic and Alpine Research, University of Colorado, Boulder, CO 80309, USA

[3] Department of Climate and Space Sciences and Engineering, University of Michigan, Ann Arbor, MI, 48109, USA

Contents of this file

Introduction

Supporting information that includes additional figures and tables that describe the statistical methods applied and results from the simulations presented in the paper.

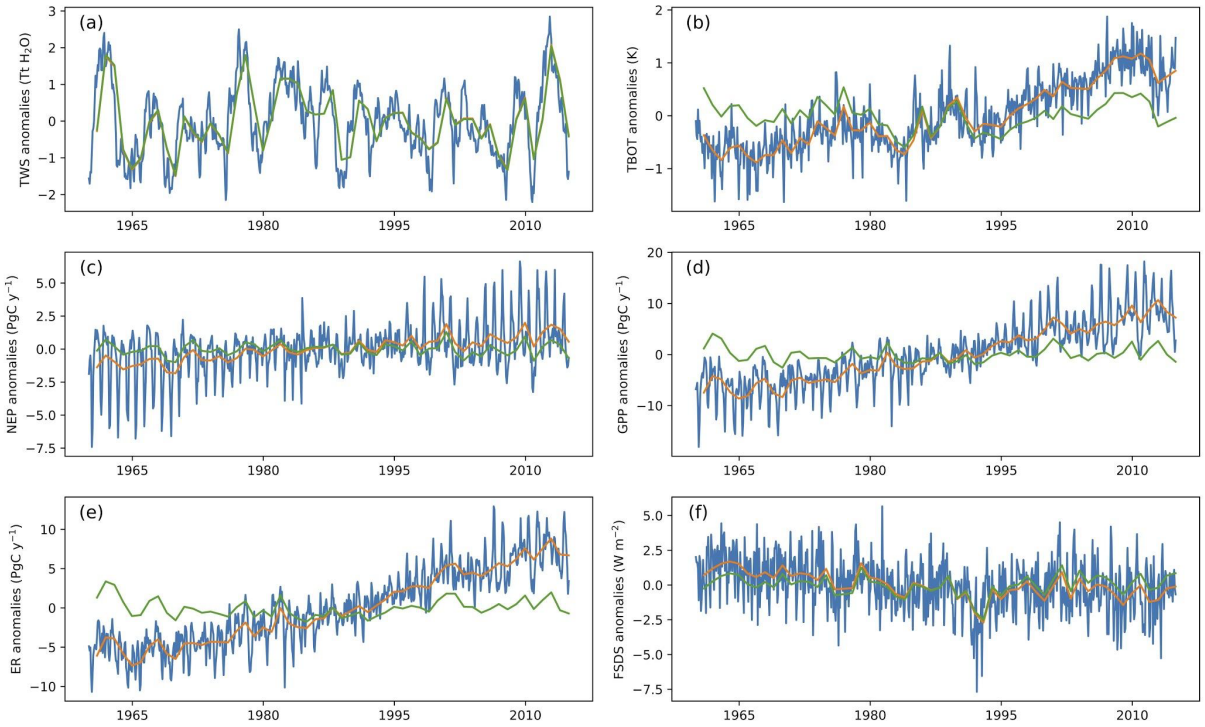

Figure S1. Global monthly anomalies, annual anomalies, and detrended annual anomalies (blue, orange and green lines respectively). Panels show variability in globally summed: (a) terrestrial water storage (TWS); (b) Air temperature (TBOT); (c) Net ecosystem production (NEP); (d) Gross primary productivity (GPP), (e) Ecosystem respiration (ER); and (f) incoming solar radiation (FSDS simulated by CESM-esm over vegetated terrestrial grid cells over the end of the historical period (1960-2014).

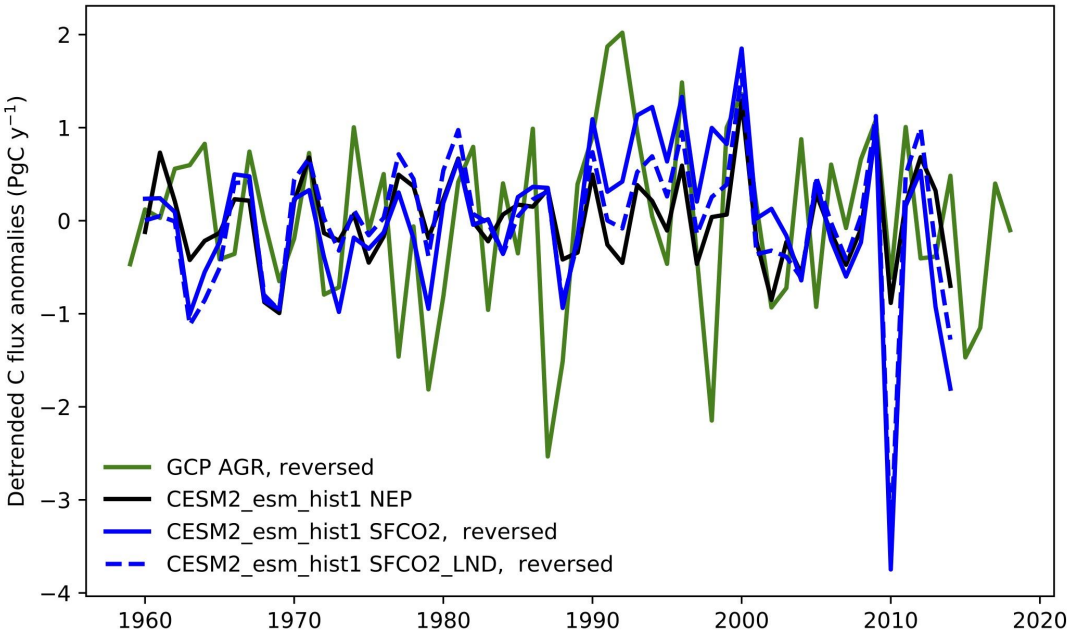

Figure S2. Detrended annual anomalies of global carbon fluxes showing the dominance of terrestrial carbon fluxes of the total IAV of net carbon fluxes simulated by CESM. As in Fig. 1, we show the atmospheric CO_2 growth rate reported by the global carbon project (green line; Friedlingstein et al. 2019), net ecosystem production (NEP) simulated CESM2-ESM (black line), the IAV of the total CESM2 surface CO_2 flux (solid blue line), and the IAV of surface CO_2 flux from terrestrial ecosystems (dashed blue line). Differences between the total surface and land CO_2 fluxes (solid and dashed blue lines) show the influence of IAV in ocean fluxes simulated by CESM2. Differences between land CO_2 flux and NEP show the effect of fire and land use change on terrestrial carbon fluxes. Note, for convenience we inverted the sign of the atmospheric growth rate and surface CO_2 fluxes (green and blue lines) so that positive anomalies show net land C uptake for all fluxes.

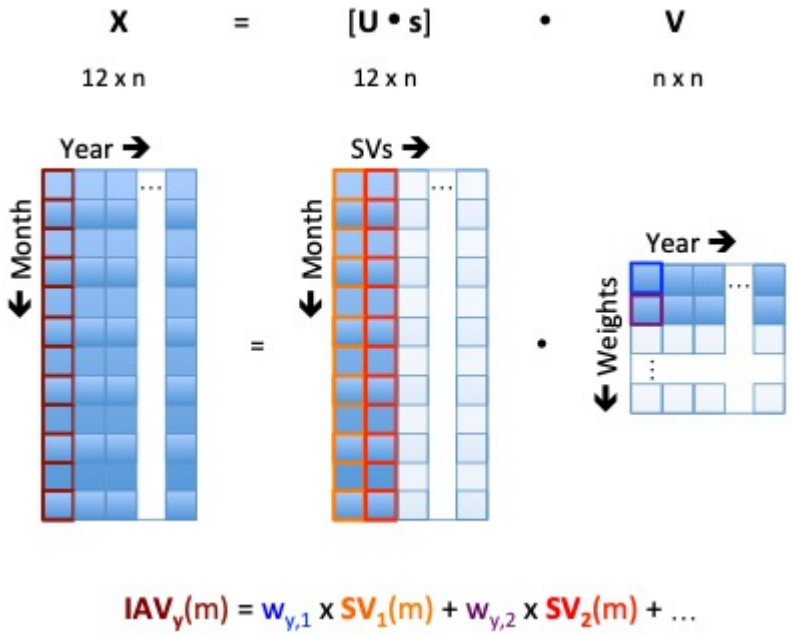

Figure S3. To decompose the annual cycle of detrended GPP time series simulated in each terrestrial grid cell, we used a singular value decomposition method (SVD; Golub and Reinsch 1971; see also Butterfield et al. 2020). The SVD method applied to a 12 x 55 matrix (12 months by 55 years included in our analysis) of annual GPP anomalies (IAV_y) resulted in three matrices, U, s, and V, the middle of which is a 55 x 55 diagonal matrix. The product of U and s provided a matrix of singular vectors (SV_i), the elements of which reflect the month (m) of year (y), that represent common seasonal patterns or modes within the data. The matrix V contained weights (wy,i) that quantify how prominent a singular vector was for any given year. Thus, the simulated IAV time series for a grid cell in any given year could be fully reconstructed as a weighted sum of singular vectors. The singular vectors are ranked by the fraction of variance they explain in the GPP time series, and the first two describe the majority (~75%) of GPP variability. Thus, we focused our analysis on only these first two singular vectors.

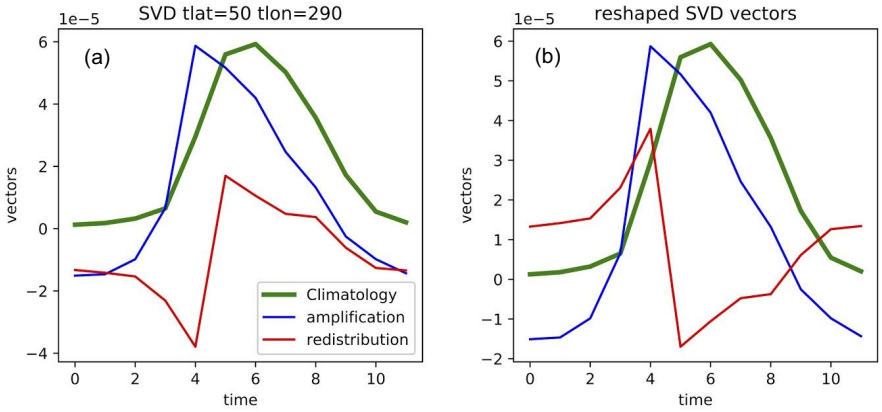

Figure S4. Example grid cell (50°N, 70°W) showing the monthly climatology of GPP fluxes (green) and SVD vectors identified as amplification and redistribution vectors (blue and red, respectively). The amplification vector was identified by its higher correlation with the monthly climatology of GPP fluxes (a). For this grid cell, the redistribution vector (as well as the associated values for weights and theta) was reversed (b), so that positive springtime anomalies occurred before the negative summer anomalies.

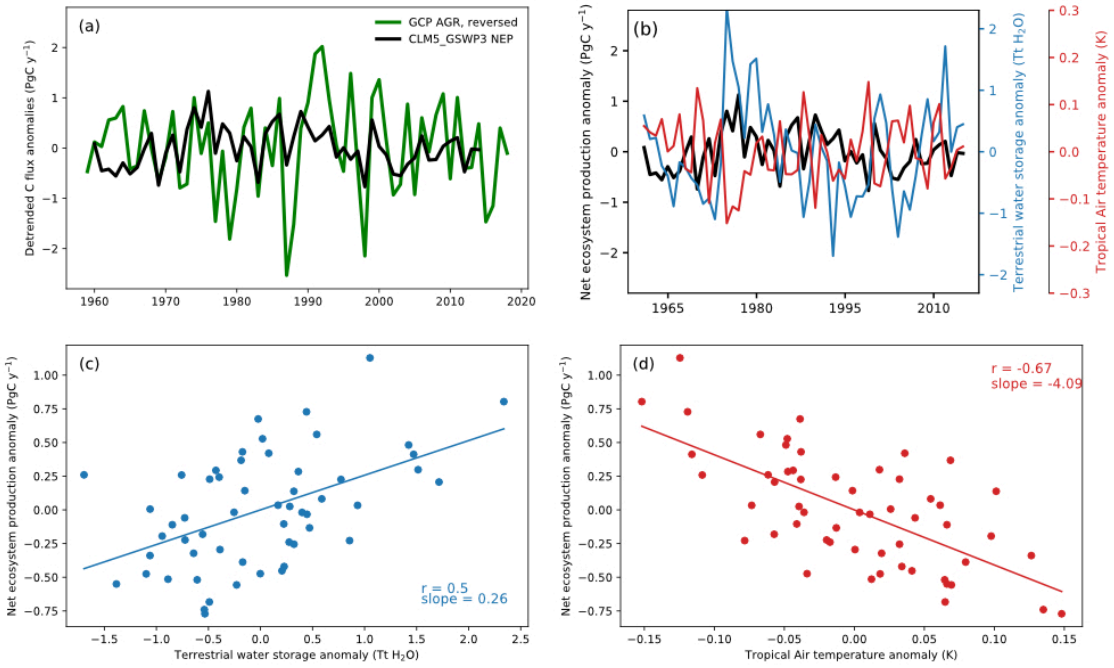

Figure S5. Detrended annual anomalies of global carbon fluxes showing low IAV for net carbon fluxes simulated by offline CLM5 simulations forced with GSWP3 climate reanalysis data through 2014 (see Lawrence et al. 2019). As in Figures 1 and S2, we show the atmospheric CO_2 growth rate reported by the Global Carbon Project, diagnosed from net biome production simulated by an ensemble of land models (green line; Friedlingstein et al. 2019), net ecosystem production (NEP) simulated CLM5 (black line). Although the model captures the sign of terrestrial carbon cycle IAV observed in the atmospheric record, it does not simulate the appropriate magnitude of response to the 1986-87 or 1997-98 El Niño events. Note, for convenience we inverted the sign of the atmospheric growth rate (green line) so that positive anomalies show net land C uptake for all fluxes.

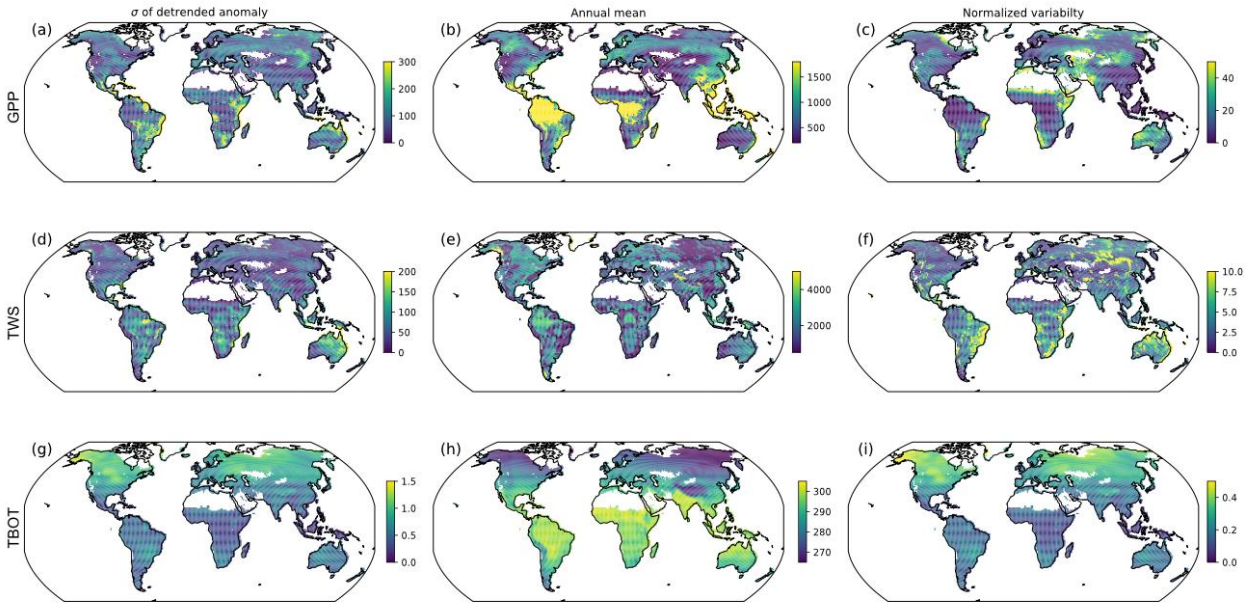

Figure S6. Characterization of GPP (top row), terrestrial water storage (TWS, middle row), and air temperature (TBOT, bottom row) simulated by CESM2-ESM. The first column (a, d, g) shows the standard deviation of detrended annual anomalies (units: gC m^{-2} y^{-1}, kg H_2O m^{-2}, and K, respectively) The second column (b, e, h) shows the annual mean simulated between 1960-2014 (units: gC m^{-2} y^{-1}, kg H_2O m^{-2}, and K, respectively). The third column (c, f, i) shows coefficient of variation (the units %, calculated and the quotient of first and second columns $\times$ 100).

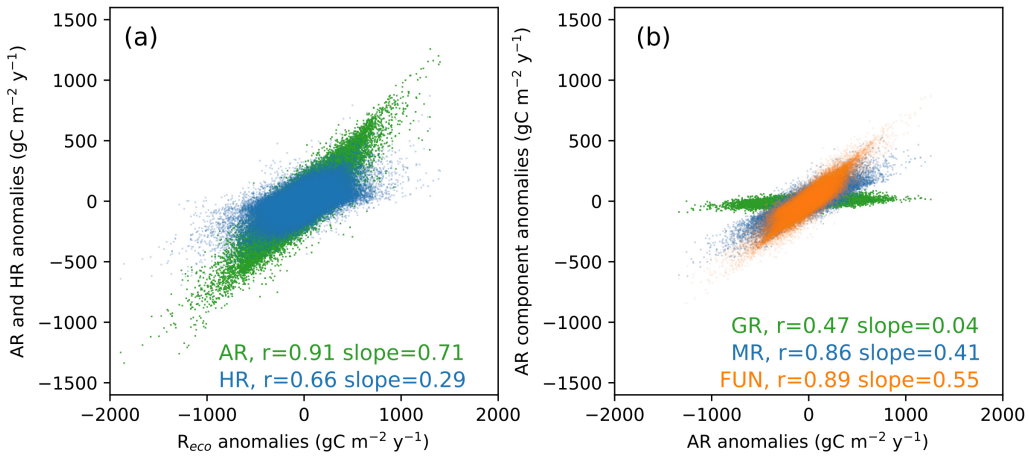

Figure S7. Gridcell correlations of annual (a) R_{eco} anomalies with anomalies of component fluxes autotrophic and heterotrophic respiration (AR and HR, respectively). Panel (b) AR anomalies with anomalies of component fluxes: growth respiration, maintenance respiration, and from the fixation and uptake of nitrogen module (GR, MR, and FUN, respectively). Correlation coefficients and slopes show that R_{eco} anomalies are most strongly correlated with AR anomalies, which are most strongly linked to the fluxes calculated by the FUN module in CESM2-esm.

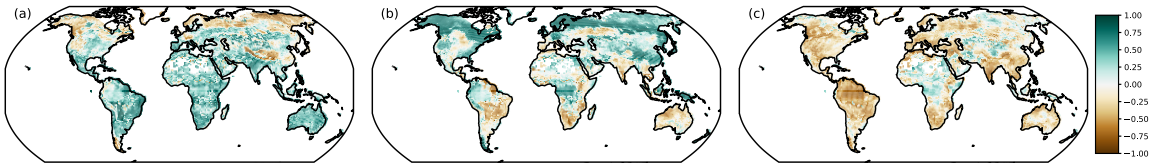

Figure S8. Correlation coefficients between detrended annual anomalies that are simulated by CESM2-esm from 1960-2014. Panels show the correlation between (a) GPP and terrestrial water storage; (b) GPP and air temperature; and (c) terrestrial water storage and air temperature. Only statistically significant correlations ($p < 0.05$, when $|r| > 0.226$ for 55 years of data) are shown.

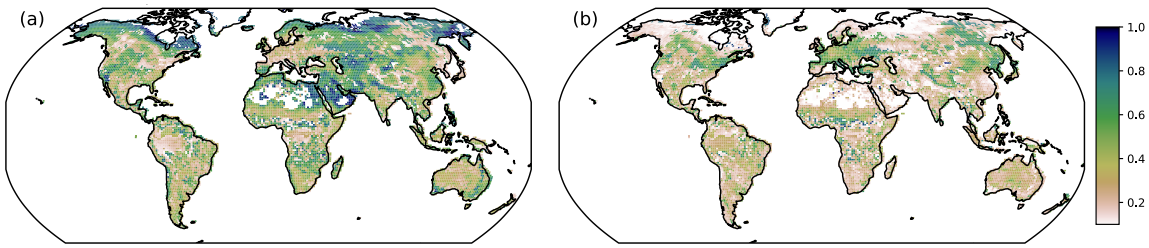

Figure S9. Fraction of variance in detrended GPP anomalies that was explained by (a) seasonal amplification or (b) seasonal redistribution vectors, as in Figure 4. Globally, these two vectors explained 45% and 29% of the variance in monthly GPP anomalies, respectively.

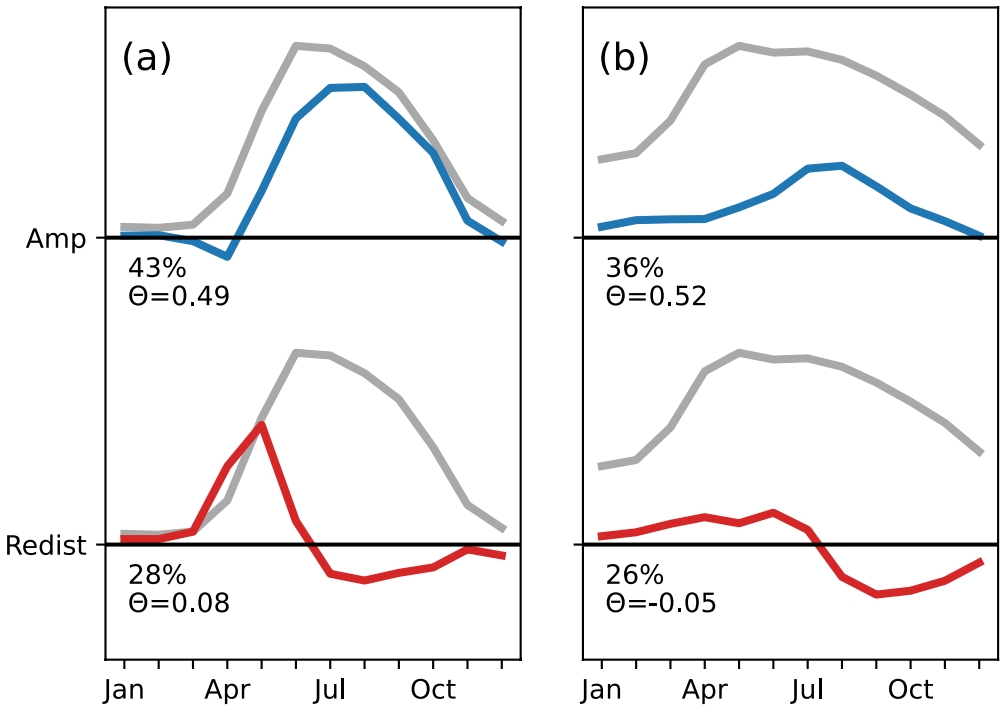

Figure S10. Zonal mean climatology of monthly heterotrophic respiration (HR) and singular vectors associated with seasonal amplification and temporal redistribution of HR (grey, blue, and red lines respectively) for the northern hemisphere. As in Figs 5-6, panels show: (a) high latitude ecosystems, 50-80°N; (b, d) northern temperate mid latitudes, 20-50°N. The magnitude of the singular vectors is arbitrary (y-axis). Mean fraction of variance explained and θ values, which indicate the net impact on the integrated seasonal signal of HR for each singular vector, are also provided.

Table S1. Coefficients of variability in four North American ecoregions defined in Butterfield et al (2020): Temperate Mixed Forest (TMF, 43°–48° N, 84°–94° W), Boreal Coniferous Forest (BCF, 54°–59° N, 94°–104° W), Midwest Cropland (MC, 39°–44° N, 86°–96° W), and Canadian Great Plains (CGP, 50°–55° N, 105°–115° W). To compare with remote sensing variability estimates reported in Butterfield et al. (2020) we define the coefficient of variability as the ratio of the interannual standard deviations to the seasonal amplitude of the multi-year mean. Both model and remote sensing results use nine years of data, 2006-2014 for the model and 2007-2015 for the remote sensing. All values are reported in %.

Region	CESM2	GOME-2 SIF	MODIS NIRv	MODIS NDVI	AVHRR NDVI
TMF	5.2	2.3	1.6	2.2	3.2
BCF	2.4	4.1	2.5	1.9	2.9
MC	1.4	1.8	2.6	2.0	1.5
CGP	2.6	2.8	3.1	2.2	2.5

Table S2. Mean Pearson's correlation coefficients between SVD weights from the amplification vectors and seasonal anomalies in GPP, terrestrial water storage, and air temperature (Fig. 7) for regions. As in Fig. 6, regions here include high-latitude ecosystems, 50-80°N; northern temperate mid-latitudes, 20-50°N, tropics, 0-20°N and 0-20°S, respectively; and southern temperate mid-latitudes, 20-50°S.

	GPP				Terrestrial Water Storage				Air temperature			
Region	**DJF**	**MAM**	**JJA**	**SON**	**DJF**	**MAM**	**JJA**	**SON**	**DJF**	**MAM**	**JJA**	**SON**
NH high	-0.45	0.22	0.95	0.41	-0.05	-0.17	-0.34	-0.21	0.21	0.38	0.38	0.13
NH mid	-0.11	0.70	0.76	0.15	0.38	0.45	0.44	0.34	-0.03	-0.26	-0.30	-0.10
NH tropics	0.50	0.67	0.67	0.45	0.54	0.59	0.50	0.40	-0.24	-0.44	-0.42	-0.27
SH tropics	0.58	0.59	0.59	0.70	0.46	0.54	0.56	0.58	-0.31	-0.32	-0.15	-0.32
SH mid	0.68	0.59	0.42	0.69	0.49	0.51	0.51	0.48	-0.38	-0.28	-0.28	-0.26

Table S3. Mean Pearson's correlation coefficients between SVD weights from the redistribution vectors and seasonal anomalies in GPP, terrestrial water storage, and air temperature (Fig. 8) for regions. As in Fig. 6, regions here include high-latitude ecosystems, 50-80°N; northern temperate mid-latitudes, 20-50°N, tropics, 0-20°N and 0-20°S, respectively; and southern temperate mid-latitudes, 20-50°S.

	GPP				Terrestrial Water Storage				Air Temperature			
Region	**DJF**	**MAM**	**JJA**	**SON**	**DJF**	**MAM**	**JJA**	**SON**	**DJF**	**MAM**	**JJA**	**SON**
NH high	-0.05	0.46	-0.11	-0.40	-0.18	-0.16	-0.24	-0.25	0.30	0.30	0.22	0.04
NH mid	0.15	0.47	-0.33	-0.41	-0.17	-0.22	-0.40	-0.32	0.33	0.31	0.33	0.21
NH tropics	0.38	0.43	0.10	-0.11	0.29	0.31	0.24	0.15	-0.13	-0.25	-0.16	-0.08
SH tropics	-0.06	0.03	0.31	0.42	0.12	0.20	0.29	0.38	-0.01	-0.13	-0.06	-0.26
SH mid	-0.30	-0.30	0.13	0.28	-0.13	-0.01	0.08	0.10	0.07	-0.01	-0.11	-0.22